

Robust Magnetometry with Single NV Centers via Two-step Optimization

Nimba Oshnik,^{1,*} Phila Rembold,^{2,3,4,5} Tommaso Calarco,^{5,3}
Simone Montangero,^{2,4,6} Elke Neu,¹ and Matthias M. Müller⁵

¹Technische Universität Kaiserslautern, Department of physics,
Erwin Schrödinger Strasse, 67663 Kaiserslautern, Germany

²Dipartimento di Fisica e Astronomia "G. Galilei",
Università degli Studi di Padova, I-35131 Padua, Italy

³Institute for Theoretical Physics, University of Cologne, D-50937 Cologne, Germany

⁴Istituto Nazionale di Fisica Nucleare (INFN), Sezione di Padova, I-35131 Padua, Italy

⁵Forschungszentrum Jülich GmbH, Peter Grünberg Institute - Quantum Control (PGI-8), D-52425 Jülich, Germany

⁶Padua Quantum Technologies Research Center, Università degli Studi di Padova, I-35131 Padova, Italy

The negatively charged nitrogen-vacancy (NV) center in diamond is a widely-used platform in the rapidly growing field of quantum technologies. In particular, NV centers near the surface of the diamond can offer nanoscale resolution as they can be brought into proximity of the sample. However, these shallow single NV centers experience considerable noise from the surface in addition to the perturbation from the spin bath in the bulk diamond crystal. This lowers the spin coherence and lifetimes leading to limited sensing capabilities. This work presents a two-step approach to improve both the spin initialization/readout and the spin manipulation processes by applying optimization algorithms to the laser and microwave controls. The goal is to increase the NV's readout contrast aiming for control pulses that are robust against power variation. With the assistance of feedback-based (closed-loop) optimization, limitations imposed by experimental imperfections and unknown system parameters are inherently considered. For pulsed ODMR-measurements, the optimization leads to sensitivities staying below $1 \mu\text{T Hz}^{-\frac{1}{2}}$ for an 83% decrease in the control power, increasing the robustness by approximately one third compared to the original sequence. Furthermore, we report sensitivities below $100 \text{nT Hz}^{-\frac{1}{2}}$ for Ramsey measurements, where optimized control pulses result in a two-fold improvement in the sensitivity. Both schemes were optimized for DC magnetic field sensing over a large range of control amplitudes. Such optimized sensing schemes are suitable for a variety of magnetometry setups that require robustness, e.g. (inhomogeneous) ensembles of NV centers, or NV scanning probes operating at different distances from the MW antenna.

I. INTRODUCTION

Quantum sensing with NV [1] centers have evolved into a prominent branch of quantum technologies in the last two decades. [2–6] NV centers serve as a multipurpose sensor for detecting magnetic [7–10] and electric fields [11], temperature [12, 13], and pressure [14, 15]. Additionally, NV centers find applications as quantum memories [16], quantum registers [17], and in several other areas of emerging quantum technologies [6]. Rapid improvement in nano-fabrication methods [18–20], material science research [21, 22], as well as control methodologies [4, 6, 23–25] have led to a variety of NV-based quantum sensors with applications in the fields of life sciences [26, 27], and material studies [28].

NV center spins are commonly initialized and read out using lasers [2, 7, 8]. Such methods rely on the optical spin state initialization and spin state-dependent fluorescence of the NV center (Fig. 3). The spin state can be manipulated with resonant magnetic microwave (MW) fields. The required MW frequency depends on the presence of static magnetic fields, which are responsible for

Zeeman splitting (Fig. 1e).

Various sensing protocols are available that make use of MW-based unitary gates, under the two-level approximation [4]. However, state-of-the-art NV-based quantum sensors do not perform on par with their theoretical potential. While the NV centers particularly close to the surface may offer high nanoscale resolution [31, 32], they also exhibit especially short dephasing and decoherence times. Likewise, limitations and errors related to the experimental setup, such as drift, finite bandwidth, and transfer functions, restrict the performance of these sensing methods. Because of the potential applications, further improvement of NV magnetometry is a flourishing and multi-disciplinary research topic [4–6].

One approach for partially compensating for these limitations involves quantum optimal control (QOC) [6, 24, 25]. QOC has previously been applied to optimize MW control pulses for quantum sensing with NV centers in a variety of settings [6, 33–38]. The diverse family of QOC algorithms is connected by its common objective: to iteratively improve a time-dependent control pulse until a given goal has been reached. Some of these algorithms rely on simulations (open-loop) to quantify the quality of the pulses, whereas others achieve the same via direct interaction with the experiment (closed-loop, Fig. 1(a-c)). Algorithms such as GRAPE [39, 40] (gradient ascent pulse engineering) or Krotov's method [41, 42]

* Current address: Universität des Saarlandes, Faculty of Natural Sciences and Technology, Physics, Campus E2.6, D-66123 Saarbrücken, Germany

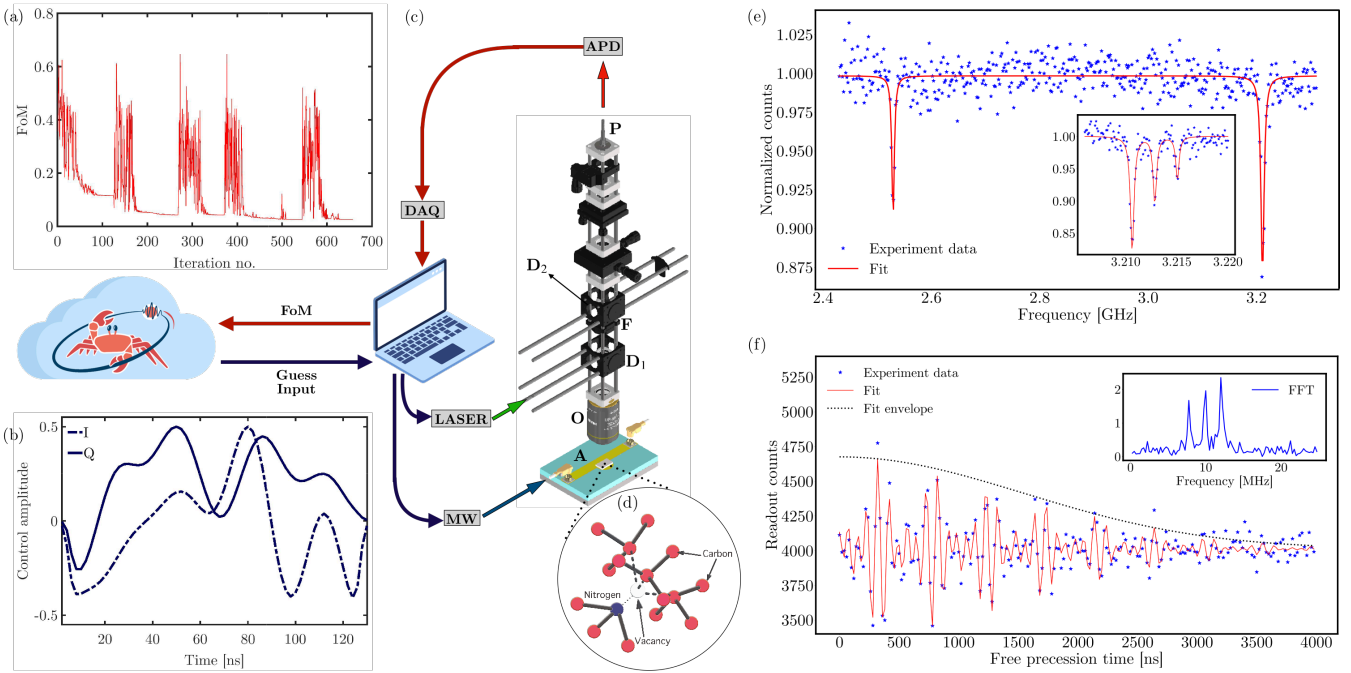


Figure 1. (color online) Schematic for the closed-loop optimization with single NV centers in diamond. The optimization algorithm suggests control pulses/parameters to the setup. The resulting figure of merit (FoM) is calculated from the output and passed back to the optimizer. This cycle repeats until the FoM converges. (a) Exemplary plot of the FoM evolution; the algorithm suggests different controls to find the global optimal solution. (b) The in-phase and quadrature components (I and Q) of a typical guess for a MW control pulse suggested by the algorithm. (c) The confocal setup used in combination with the RedCRAB optimization program; laser (green arrow) and MW (blue arrow) pulses are used to control the NV spin state. The fluorescence (red arrow) is collected with an optical fiber, P , connected to a single photon counter (APD), logged with a data acquisition device (DAQ), and further processed on the local control system to pass the FoM to the remote optimization server. (d) Lattice structure of the NV center. The NV quantization axis is shown as a dotted black line. (e) Continuous wave optically detected magnetic resonance (cw-ODMR) preformed with a single NV center in presence of an external magnetic field that leads to two resonance peaks due to Zeeman splitting, the inset figure shows the result of the low control power pulsed ODMR (non-optimized) performed around the right resonance peak for the $m_s = 0 \leftrightarrow +1$ transition. The three peaks correspond to the hyperfine transitions resulting from the electron-nuclear spin coupling. (f) Result of the Ramsey sensing sequence with single NV center using optimized control pulses shown in (b) (see section IV B), the inset figure shows the fast Fourier transform of the experimental data. (The confocal model in (c) is designed with parts adapted and modified from [thorlabs.com](#) [29] and [gradbcad.com](#) [30] with permission under terms of reuse. For details on the setup see appendix A.)

require the calculation of the derivative of the goal function (gradient-based). The dCRAB algorithm (dressed Chopped RAndom Basis) [25, 43, 44] can take a gradient-free approach. Additionally, the functional parametrization approach of the dCRAB algorithm can be combined with gradient search methods, via algorithms like GROUP [45] (gradient optimization using parametrization) or GOAT [46] (gradient optimization of analytic controls). Even with a moderate number of basis functions the control pulse can contain enough information to steer the system [47, 48].

In this work, we apply the gradient-free dCRAB approach that can readily be used with feedback from the experiment. Indeed, we present a two-step strategy to exploit the full potential of feedback-based optimization algorithms and QOC [25, 49, 50] in connection with shallow single NV centers in diamond. At the first step, the optical spin initialization/readout process is improved. The second step aims to make the spin state manipula-

tion with MW control pulses more efficient. The ultimate goal of these optimizations is to enhance the sensitivity of DC magnetometry methods described in section II. The optical laser pulse-based processes are optimized via a gradient-free Nelder-Mead search [51] in the parameter landscape corresponding to the experimental system and setup (section III A). Subsequently, the MW pulses are optimized with a gradient-free, closed-loop version of the dCRAB algorithm. The optimization routine is implemented via the QOC software package RedCRAB (Remote dCRAB) [50]. The optimized sequences are developed for two DC magnetometry methods (section III B), namely pulsed ODMR [12, 52] and Ramsey [7, 8] measurements. Different optimization bases (Fourier [53] and Sigmoid [54]) are compared to assess their suitability for the involved methods.

All optimizations include figures of merit (FoM, see Fig. 1a) based on the spin readout contrast. While the contrast has a big influence on the sensitivity it does not

capture the ultimate goal of the optimization to measure the magnetic field of a structure over a certain area. This area is limited by the inhomogeneity of the applied microwave; the larger the separation between the NV center and the antenna, the weaker the drive power. To compensate, all FoM are adapted for drive powers ranging from 100% to 20% of the maximum. Finally, the optimizations are assessed in terms of the average sensitivity enhancement and the covered area (section IV).

II. DC MAGNETOMETRY METHODS

The transitions in the energy level structure of the NV center (Fig. 3a) strongly influence its sensitivity towards external magnetic fields. The spin one triplet state which forms the ground level has a zero-field splitting (ZFS) of ≈ 2.871 GHz. In presence of an external magnetic field along the NV center's axis, Zeeman splitting lifts the degeneracy between the $m_s = \pm 1$ states. This splitting provides a direct way to quantify the field along the NV quantization axis (B_{NV}). A pseudo two-level system can be constructed from the $m_s = 0$ and one of the $m_s = \pm 1$ states. This two-level approximation forms the basis for the DC magnetometry techniques explored in this work, i.e., pulsed ODMR and Ramsey method.

The simplest procedure to detect magnetic fields is called continuous wave optically detected magnetic resonance (cw-ODMR) [52, 55]. The method involves a laser continuously polarizing the NV spin state, while MW pulses with different drive frequencies are applied sequentially to locate the resonance peaks. The splitting between the resonance peaks is proportional to B_{NV} . Cw-ODMR measurements are less demanding in terms of experimental resources and complexity in comparison to pulsed measurement schemes, as they do not require pulsed controls. However, by nature, continuous-wave measurements have a lower spin readout fidelity and suffer from optical and MW power broadening [52].

The dephasing time T_2^* sets a limit to the achievable sensitivities with different DC magnetometry methods (see appendix C, Eq. (C4)). Short laser and MW pulses help to overcome the power broadening effect [52] and to reach better sensitivities. Pulsed ODMR involves pulsed optical excitations and spin state transfer using MW π -pulses. For shallow NV centers, the spin states decay quickly. Hence, pulsed ODMR experiments with short, high power control pulses provide an advantage. The short control pulses inherently result in faster measurements, which lead to an improvement in the overall sensitivity (see appendix C). The pulsed ODMR method also offers enhanced readout contrast, which further improves the sensitivity towards resonance frequency (detuning).

Measurements of the magnetic field over an extended area suffer from the different relative distances between MW antenna and NV center, if they are moved separately. As the MW field decays with distance from the antenna, this is translated into a variation in control power

for the NV center. Hence, applications involving certain diamond-based scanning probes, or an ensemble of NV centers benefit from pulses that are robust against control amplitude variation. The design of our control strategy specifically enforces robustness against such variations.

ODMR measurements based on high MW power suffer from power broadening of the resonance profile. [52] In general, the ODMR method does not exploit the quantum property of spin superposition, which provides a way to make the measurements more sensitive [4]. Conversely, the double-pulse-based Ramsey sequence does. It also has the advantage of avoiding the mentioned broadening effects [56]. For the Ramsey method, the single spin transferring π -pulse is substituted with two $\frac{\pi}{2}$ -pulses. The optically initialized NV spin state is transferred into a superposition state by the first of the two $\frac{\pi}{2}$ -pulses. This superposition state interacts with the external magnetic field for a finite time τ , thus accumulating a phase. Eventually, the second $\frac{\pi}{2}$ -pulse converts the accumulated phase into an optically measurable population difference. In contrast to the ODMR-based frequency-sweep methods, the Ramsey sensing protocol is performed at a fixed drive frequency of the control field. In addition, τ can be varied to measure minimal fluctuations in external magnetic fields [4]. In general, the Ramsey method can be used to sense any magnetic fields that changes slowly enough i.e., with frequencies less than $\frac{1}{\tau}$.

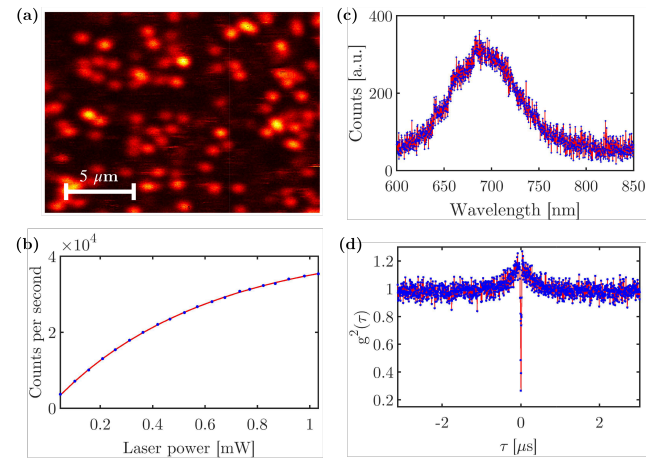


Figure 2. (color online) Sample characterization; (a) Confocal scan of the diamond sample with shallow single NV centers. (b) Count rate of a single NV vs. power of the excitation laser. The saturation behavior can be studied to obtain the excitation power with the best signal-to-background ratio for the experiments. Ideally this lies below the saturating laser power. (c) Typical emission spectra of the single NV centers in the sample. The NV charge states have different spectral signature, the given spectra indicates negatively charged NV state. (d) Exemplary second order correlation measurement, which is performed to identify single NV centers in the sample ($g_2(0) \approx 0.27$).

A. Sample and Experimental Setup

All experiments in this work are performed using an electronic-grade diamond sample ($300\text{ }\mu\text{m} \times 100\text{ }\mu\text{m} \times 40\text{ }\mu\text{m}$) with implanted NV centers (Fig. 2). The ion implantation was performed with a fluence of $3 \times 10^{11}\text{ cm}^{-2}$ at 600 keV followed by annealing (850°C), which disperses the defects leading to a uniform NV center distribution in the sample. Afterwards, a second oxidation annealing at 400°C was performed followed by tri-acid cleaning to reduce the NV density and obtain shallow single NV centers at around 5-10 nm below the surface. The average NV density is estimated to be around $7 \times 10^7\text{ cm}^{-2}$. The value is obtained by analyzing confocal scans of the sample surface (see Fig. 2a).

For the experiment, the sample is mounted on an omega-shaped strip-line antenna (Fig. 1c, A)[57]. The antenna delivers the MW control pulses and is mounted on a piezoelectric scanner to perform multi-axial scans. The dichroic mirrors (Fig. 1c, D_1 and D_2) filter the excitation laser pulse and direct the fluorescence along the collection arm of the confocal setup. Additionally, a 600 nm long-pass filter (Fig. 1c, F) in the collection arm is used for spectral filtering. The optical initialization and readout are assisted by an objective (Fig. 1c, O), which delivers and collects the light to/from the in-focus diamond sample containing shallow single NV centers. Laser pulsing is achieved with a digitally modulated diode laser (modulation bandwidth: 125 MHz). The MW control pulses are generated by mixing the in-phase (I) and quadrature (Q) components (Fig. 1b) with a carrier signal. The resulting pulse is subsequently amplified and delivered to the confocal setup via the strip-line antenna. For more details on the setup, see appendix A.

III. OPTIMIZATION METHODS

The sensing protocols described in section II rely on the efficiency of two types of control: Readout/initialization via the laser and spin manipulation via the MW field. In this section, two complementary optimization strategies are presented, both using the RedCRAB optimization suite. The first (section III A) adapts the laser pulse parameters and the second (section III B) the MW control pulses. The software allows for smooth communication between the remote experimental setup and the server-based optimizer. It also incorporates additional features like amplitude limitation, bandwidth restriction, and several other parameters reflecting the accuracy and limitations of the experimental setup. Thus the essential requirements for both optimizations are straightforwardly incorporated within RedCRAB.

In both steps of the optimization, we first have to identify and quantify the goal with a figure of merit (FoM) that can be measured in the experiment. Subsequently, the controllable parameters of the system are identified.

In each iteration of the few-parameters direct search, the algorithm sends a new set of parameters to the system, which in turn calculates the corresponding FoM and passes it back to the algorithm. This process repeats until the desired goal is achieved. In the QOC step, instead of optimizing static parameters by direct search, we optimize time-dependent control pulses via the dCRAB algorithm [25, 43, 44, 50].

A. Parameter optimization for Spin State Initialization and Readout

Strong spin polarization and spin state dependent fluorescence are fundamental to the readout of single NV centers. These properties primarily originate from the transition rates of the spin preserving radiative and the non-radiative decay channels between the NV energy levels (see Fig. 3a). The dominant decay via the metastable state leads to a brighter signal from the spin state with $m_s = 0$ than with $m_s = \pm 1$ (see Fig. 3c).

The primary limitation to an efficient optical readout of the NV spin state comes from the photon shot noise. Consequently, the statistical determination of the spin state requires an averaged readout over a large number of experimental repetitions. The spin state readout fidelity \mathcal{F} for such probabilistic measurements is expressed in terms of the noise parameter σ_R [10, 58]:

$$\frac{1}{\mathcal{F}} = \sigma_R \approx \sqrt{1 + \frac{2(R_0 + R_1)}{(R_0 - R_1)^2}}, \quad (1)$$

such that $\mathcal{F} = 1$ at the spin projection noise limit of the sensitivity (see appendix C). R_1 (R_0) is the total number of collected photons from the readout of the spin state initialized in $m_s = \pm 1$ ($m_s = 0$). Experimentally, the readout contrast C is given by

$$C = \frac{R_0 - R_1}{R_0 + R_1}. \quad (2)$$

Its relation to \mathcal{F} is given in appendix C. Intrinsically, the contrast depends on several system properties and experimental parameters,

$$C \equiv C[\gamma_{ij}, \mathcal{L}_p, \mathcal{L}_d, \Omega_R, B_\perp, E_{xy}, T, \dots], \quad (3)$$

where γ_{ij} is the transition rate between levels $i \leftrightarrow j$, \mathcal{L}_p is the laser pulse intensity, \mathcal{L}_d is the laser pulse duration, Ω_R is the amplitude of the spin inversion control pulse, B_\perp and E_{xy} are off-axial magnetic and electric field components at the position of the NV center respectively, and T is the ambient temperature. In addition, there are several other factors including crystal field strain and charge state stability that may affect the fluorescence of the NV center, and ultimately influence the readout contrast. The majority of the parameters in Eq. (3) depend on the system properties, material characteristics, and ambient conditions that are generally not fully controllable. In

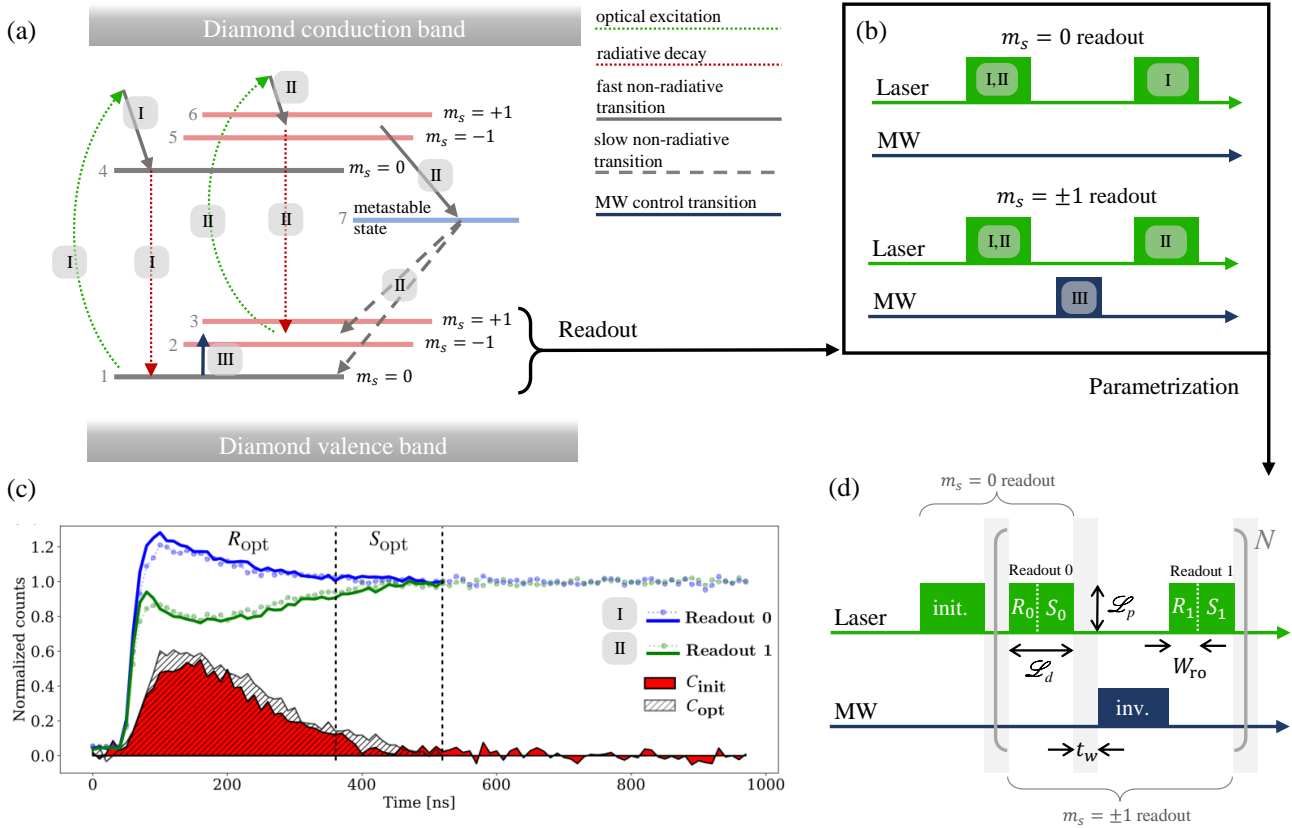


Figure 3. (color online) Initialization and readout of the NV spin state. (a) The energy level structure of the NV center ($S = 1$) within the diamond bandgap. A green laser pulse ($\lambda = 520\text{--}530\text{ nm}$) excites the NV center. This excitation process is primarily spin conserving. The excited $m_s = 0$ spin state (4) has a higher probability to radiatively decay to the ground level $m_s = 0$ state (1), denoted as path I. If the system is initially in the ground state $m_s = \pm 1$ (2, 3), the excitation is followed by a decay via the metastable state (7), as shown in path II. (b) A laser pulse polarizes the system to the ground level $m_s = 0$ state via paths I and II (spin state initialization). If no MW is applied ($m_s = 0$ readout), the NV center remains in the same state. However, a MW pulse (shown under $m_s = \pm 1$ readout) can transfer the spin state to the ground level $m_s = \pm 1$ states (path III). (c) Path II leads to a drop fluorescence because of the decay via the long-lived metastable state. The fluorescence count rate allows for differentiating the spin states during optical readout. The dashed curves with dots show a typical readout signal with a 1 ps laser pulse for different initial spin states (blue: $m_s = 0$, green: $m_s = \pm 1$). The solid curves indicate the optimized spin state readout (see section III A). The filled areas denote the readout contrast (Eq. (2)) obtained with the 1 ps laser pulse (C_{init} , red) and the optimized readout (C_{opt} , striped). R_{opt} and S_{opt} indicate the optimized windows for the readout and saturation respectively. (d) Parameters for the optical readout optimization. \mathcal{L}_p and \mathcal{L}_d are the laser power and duration respectively. W_{ro} is the readout window, t_w is the wait time after each laser pulse. R_i and S_i correspond to the photon collection windows described in Eq. (5). A spin inverting rectangular MW pulse (inv.) is used for the parameter optimization. Readout 0 (1) corresponds to the readout of the $m_s = 0$ (± 1) spin states. After an initial laser pulse (init.), each measurement is repeated N times to enhance the signal to noise ratio.

practice, some of the system properties can be characterized before the optimization of the readout contrast. For example, the charge state of the NV center can be determined from the emission spectrum (Fig. 2b). Similarly, external factors such as crystal field strain and temperature directly influence the ZFS of the NV center. In this regard, pre-characterized single NV centers (Fig. 2c) with ZFS $\approx 2.871\text{ GHz}$, and stable photoluminescence that do not exhibit charge state related blinking allow to fully exploit the scope of laser pulse parameter optimization. Likewise, a well-aligned static magnetic field B_{NV} is a prerequisite for the optimizations performed in presence

of a magnetic bias field. It is noteworthy that photons originating from NV^0 can be filtered from the readout signal (Fig. 1a). As a result charge state instability leads to blinking of the NV fluorescence signal [59].

Other experimental parameters in Eq. (3) such as \mathcal{L}_p and \mathcal{L}_d , directly influence the optically induced transitions, as well as the charge state stability [58, 59]. In contrast, the effect of the wait time t_w (see Fig. 3d) between the pulses is more indirect. Hence, it is commonly set to ca. 300 ns, which corresponds to the lifetime of the metastable state [60]. Similarly, the photon collection window W_{ro} is often calculated in advance to obtain the

best SNR for every readout [3]. Consequently, Eq. (3) can be reduced to a simpler form based on the variables that can be controlled experimentally,

$$C \sim C[\mathcal{L}_p, \mathcal{L}_d, W_{\text{ro}}, t_w, \Omega_R]. \quad (4)$$

Although it is not straightforward to find an analytical form to characterize the dependence of C on these parameters, they can be directly adjusted in a closed-loop optimization on the experiment. Figure 3 shows the two-shot scheme for the contrast measurement used in the optimization routine. Each laser pulse (Readout 0 (1)) is divided into a spin readout window R_0 (R_1), and a spin state saturation window S_0 (S_1). Their durations are determined by the optimization parameters \mathcal{L}_d and W_{ro} . A spin inversion MW pulse flips the spin state between the laser pulses. The FoM, which is minimized during the optimization, is given by

$$\text{FoM}_{\text{RO}} = 1 - \bar{C} \left[1 - \text{var} \left(\left| \frac{S_0 - S_1}{S_0 + S_1} \right| \right) \right]. \quad (5)$$

Here, \bar{C} is the readout contrast averaged over N experimental repetitions as shown in Fig. 3d. In addition to maximizing the readout contrast in the spin readout windows, FoM_{RO} also ensures uniform spin state initialization, as the optimized value tends to minimize the variance in the photon counts from the two spin states in the saturation windows (Fig. 3).

The closed-loop optimization of readout parameters is generally relevant for a variety of methods, such as readout-based on spin-to-charge-state conversion [58] and photoelectric readout [61], which inherently involves laser pulses. Furthermore, the optimized readout can be integrated directly with MW-free, all-optical magnetometry methods [62].

B. Quantum Optimal Control for Spin State Manipulation

An optimally initialized spin state and its efficient read-out are two of the essential criteria for a practical quantum sensor [4]. In addition, the spin state has to be controlled accurately to implement a sensing protocol. In this subsection, we study the optimization of MW control pulses for spin inversion and for a $(\frac{\pi}{2})_x$ -gate via the dCRAB algorithm [25, 43, 44, 50].

Before proceeding to the specifics of the optimization schemes, we discuss the dynamical equations of the system to introduce the basic concept of QOC. The system is described by the constant drift Hamiltonian H_d , and the control Hamiltonians H_c^i , which are modulated by control pulses $u^i(t)$:

$$\begin{aligned} H(t) &= H_d + \sum_i H_c^i u^i(t) \\ &= \frac{\hbar}{2} (\Delta \sigma_z + \sigma_x u^1(t) + \sigma_y u^2(t)), \end{aligned} \quad (6)$$

where the complete Hamiltonian $H(t)$ is given in the rotating wave approximation (RWA) with the detuning Δ , the Pauli matrices σ_i , and the controls $u^1(t) = \Omega \cos(\phi)$ and $u^2(t) = \Omega \sin(\phi)$. These controls correspond to the in-phase and quadrature components of a MW drive with Rabi frequency $\Omega(t)$ and phase $\phi(t)$ applied for the duration t_p .

The control objective for the MW pulses is to efficiently transfer the initial spin state $|\Psi_i\rangle$ to the final state $|\Psi_f\rangle$. Hence, the FoM is defined as the state fidelity,

$$\mathcal{F}_p = |\langle \Psi_f | U(t) | \Psi_i \rangle|^2, \quad (7)$$

$$\text{where } U(t) = \exp \left[-\frac{i}{\hbar} \int_0^{t_p} H(t) dt \right]_{\text{(to)}}. \quad (8)$$

The subscript (to) indicates a time-ordered exponential propagator. At this point, the FoM is a functional of the control pulses. The controls are subsequently parametrized by a set of $N_{\text{set}} \times M$ basis elements $f^i(\omega_n; t)$. Each element is defined by its superparameter ω_n , which is randomly selected from $\omega_{\min} < \omega_n < \omega_{\max}$, where ω_{\min} and ω_{\max} are the minimum and maximum allowed values. The number of basis functions M per superparameter depends on the basis. These superparameters can be the frequencies of a set of trigonometric functions (Fourier basis [44]; in this case ω_{\min} and ω_{\max} set the allowed bandwidth of the control pulse) or the offsets for a set of step functions (Sigmoid basis [54]). The resulting pulses take the following form:

$$u^i(t) = u_0^i(t) + \sum_n \sum_i A_n f^i(\omega_n; t). \quad (9)$$

Here, $u_0^i(t)$ represents the initial guess for the pulse.

Following the parametrization, the goal of the QOC routine is to find the optimal values for the coefficients A_n , maximizing the FoM (Eq. (5)). Especially in closed-loop optimization, only a limited number of parameters can be optimized at a given time. Therefore, additional steps are required to avoid local optima. The dCRAB algorithm tackles this issue by switching the set of basis elements every time the optimization has converged under the given constraints [44]. Every new optimization (superiteration) is started with the previous optimum as an initial guess i.e. $u_0^i(t) = u_{\text{opti}}^i(t)$.

The first MW optimization presented here concerns the spin-inversion pulse in the pulsed ODMR sequence (see Fig. 3). As the fidelity cannot be obtained directly from the experiment, the efficiency of the spin state transfer is estimated through the optical readout contrast C (Eq. (3)). The previously obtained parameters for the laser-based initialization/readout are used as the default for the MW control pulse optimization experiments. To achieve robustness, the control field amplitude variation is incorporated in the FoM by averaging the contrast over

a range of Rabi frequencies.

$$\text{FoM}_{\text{podmr}} = 1 - \frac{1}{N_p} \sum_k^{N_p} \left(\frac{R_0^k - R_1^k}{R_0^k + R_1^k} \right), \quad (10)$$

where N_p is the total number of sampled amplitudes and R_i^k are the photon counts from the corresponding spin state collected during Readout 0 (1) (see Fig. 3). The goal of the optimization is to minimize $\text{FoM}_{\text{podmr}}$.

The Ramsey protocol does not involve spin inversion but instead a $(\frac{\pi}{2})_x$ -gate. In the sensing procedure, this pulse maps the spin eigenstates to a superposition state with a given phase on one hand and the phase back to a spin population on the other hand. Gates cannot be straightforwardly quantified using the contrast. Instead, their quality is commonly quantified via gate tomography, which requires additional state preparations and related measurements. We develop a protocol to translate its unitary properties into a readout contrast that takes the same amount of measurements as the evaluation of the spin state inversion. Previous optimizations for D-Ramsey pulse sequences with NV centers were performed in an open open-loop scheme using a cooperative design. [13] Figure 4 shows the scheme connecting the pulse performance to the readout fluorescence contrast C from two spin states. Similar to the case of pulsed ODMR, the figure of merit is defined as

$$\text{FoM}_{\text{ram}} = 1 - \frac{1}{N_p} \sum_k^{N_p} \left(\frac{\mathcal{P}_0^k - \mathcal{P}_1^k}{\mathcal{P}_0^k + \mathcal{P}_1^k} \right), \quad (11)$$

where \mathcal{P}_i^k is the photon count for the k^{th} amplitude value after projection into spin state i . The photon counts \mathcal{P}_i^k are related to the spin transfer to the different states using the following series of transformations,

$$\begin{aligned} U(t_p) \pi_x U(t_p) &\mapsto \mathcal{P}_0, \\ U(t_p) U(t_p) &\mapsto \mathcal{P}_1, \end{aligned}$$

where $U(t_p)$ is the parametrized unitary operator for the optimized control pulse of duration t_p , and π_x denotes the unitary transformation for the rectangular π -pulse applied along the x -axis. The maximization of the contrast ideally corresponds to the following conditions:

$$|\langle 0 | U(t_p) \pi_x U(t_p) | 0 \rangle|^2 = 1, \quad (12)$$

$$|\langle 1 | U(t_p) U(t_p) | 0 \rangle|^2 = 1. \quad (13)$$

Here, $|0\rangle$ and $|1\rangle$ denote the two spin states of the system under the two-level approximation: $|0\rangle$ is given by the $m_s = 0$ state and $|1\rangle$ represents either $m_s = +1$ or $m_s = -1$ depending on the corresponding experiment specified in section IV. We introduce the parametrization of the unitary transformation generated by the control pulse as

$$U(t_p) = \exp \left[-i \sum_j c_j \sigma_j \right], \quad (14)$$

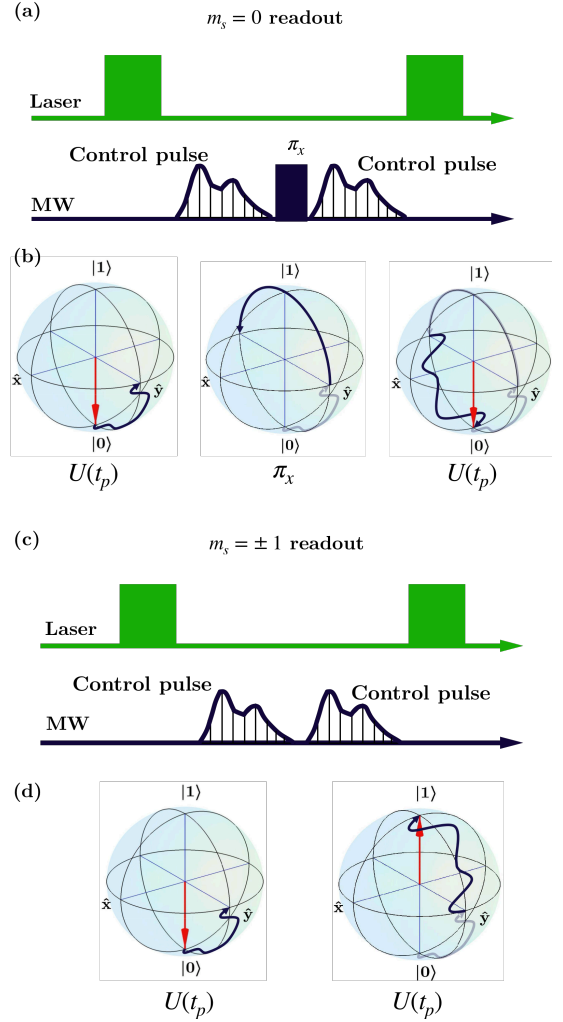


Figure 4. (color online) Measurement protocol for the Ramsey sequence optimization. The spin is projected into $m_s = 0$ and $m_s = \pm 1$, similarly to the spin state measurement in Fig. 3b; (a) for the $m_s = 0$ spin state projection (state $|0\rangle$), a known refocusing unitary π_x -gate (solid fill) is used between the finite duration optimized pulses $U(t')$ (dashed fill). (b) shows an exemplary Bloch sphere representation of an optimized pulse scheme from (a). The red arrows indicate the initialized and final spin state and blue lines denote the path traced by the spin state on the Bloch sphere under the influence of the MW pulses. (c) In the absence of the intermediate π -pulse, the spin state is ideally transferred into the $m_s = \pm 1$ (state $|1\rangle$). (d) shows an exemplary Bloch sphere representation of the optimized pulse scheme in (c), consecutive application of the guess pulse ideally leads to optimized spin state transfer.

with coefficients c_j for $j = \{x, y, z\}$, and $\hat{c}_j = c_j/c$, with $c = \sqrt{c_x^2 + c_y^2 + c_z^2}$. Then, Eq. (13) implies

$$1 = \sin^2(2c)(\hat{c}_x^2 + \hat{c}_y^2) \quad (15)$$

and thus $c = \frac{1}{2}(\frac{\pi}{2} + k\pi)$, for integer k , and $c_z = 0$.

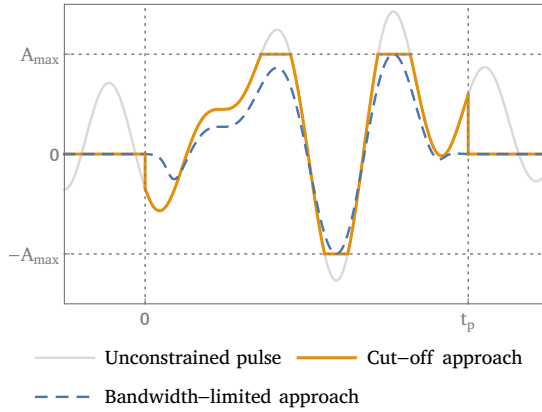


Figure 5. Restriction approaches. The unconstrained pulse may either be cut off at the amplitude $\{-A_{\max}, A_{\max}\}$ and time $\{0, t_p\}$ limits ("cut-off approach") or shifted and rescaled to fit within the available window ("bandwidth-limited approach").

Substituting this into Eq. (12) gives

$$1 = 4\hat{c}_x^2 \sin^2 c [\cos^2 c + \hat{c}_z^2 \sin^2 c] = \hat{c}_x^2, \quad (16)$$

finally indicating that $c_x = c = \frac{1}{2}(\frac{\pi}{2} + k\pi)$, and hence $c_y = 0$. In other words, FoM_{ram} in Eq. (11) is minimized for a $\frac{\pi}{2}$ rotation around the x -axis (in the positive or negative direction):

$$U_{\text{opti}}(t_p) = \exp \left[-\frac{i}{2} \left(\frac{\pi}{2} + k\pi \right) \sigma_x \right]. \quad (17)$$

The optimization of the MW pulses is performed with both, the Fourier and Sigmoid basis separately. To ensure the amplitude and duration are limited (i.e., that the amplitude stays within an upper and a lower limit and the pulse is zero at $t = 0$ and $t = t_p$), two different strategies can be applied, as illustrated in Fig. 5. In the cut-off approach, the pulses are cut off at $t = 0$ and $t = t_p$ to ensure that the pulse is zero outside the specified time interval. Similarly, they are cut off at the top and bottom to implement the amplitude limits. Instead, the bandwidth-limited approach consists of re-scaling the pulse in order to fit within the amplitude limits, followed by multiplying it with a smooth window function like a flat-top Gaussian to avoid discontinuities at initial and final time.

In the cut-off approach (see Fig. 5), the Fourier basis is expected to produce a lot of high-frequency components when the optimization algorithm maximizes the pulse area. Conversely, in the bandwidth-limited approach the Fourier basis will have difficulties to significantly expand the pulse area. At the same time, the Sigmoid basis has the ability to exploit the pulse area without producing high frequencies [54] when combined with the bandwidth-limited approach. The inherent smoothness offered by the Sigmoid basis (see appendix B) provides a particular advantage for frequency-sweep-based spectroscopic measurements, where spurious harmonics are to be avoided.

IV. EXPERIMENTAL RESULTS AND SENSITIVITY ANALYSIS

A straightforward way to test the general applicability of the optimization strategies discussed in the preceding section is to apply them to different single NV centers and compare the readout contrast enhancement on a case-specific basis. In addition, the average sensitivities from the experiment quantify the optimization benefits. In the proceeding section, the optimization schemes from section III are implemented and compared. First, we assess the improvements resulting from optimized readout (OR) (section IV A), and the additionally optimized spin transfer pulses (section IV B) for the pulsed ODMR method. Second, OR is applied with optimized control pulses for the Ramsey protocol and the results are discussed in section IV C. Both amplitude restriction approaches (Fig. 5) are implemented in the optimizations. We use three different NV centers, NV1, NV2 and NV3 (see table I). All results involving NV1 and NV2 are obtained with the cut-off restriction, while NV3-related optimizations use the bandwidth-limited approach. The robustness of the pulses is tested over a range of control power varying from maximum to the 10% of the maximum control power. This variation is artificially introduced in the experiment by changing the power at the MW source.

A. Initialization and Readout

Experimental restrictions are directly included in the closed-loop optimization of the initialization and readout process by limiting the optimization parameters. The bounds on the parameter set $\{\mathcal{L}_p, \mathcal{L}_d, W_{\text{ro}}, t_w\}$ are given as:

$$\begin{aligned} \mathcal{L}_p &\in [2, 40] \text{ (mW),} \\ \mathcal{L}_d &\in [300, 2000] \text{ (ns),} \\ 0.25 \mathcal{L}_d &\leq W_{\text{ro}} \leq 0.75 \mathcal{L}_d \text{ (ns),} \\ \text{and } t_w &\in [0, 1000] \text{ (ns).} \end{aligned}$$

Limits on \mathcal{L}_p correspond to the available source laser power. The initial guess for the optimization is chosen to be $\{\mathcal{L}_p \leq P_{\text{sat}}, 1000 \text{ ns}, 450 \text{ ns}, 300 \text{ ns}\}$, where P_{sat} is the saturation laser power for the single emitter). In cases where the saturation limit cannot be reached with the available laser intensity, the initial guess is obtained by considering the saturation curve (Fig. 2b) to identify the approximate laser intensity with the most favorable signal-to-background ratio. The main readout optimization results are summarized in table I. As a general observation, the optimized laser pulses are shorter than the corresponding initial guesses, while t_w values do not change profoundly during the optimization. Moreover, reduction of the measurement time improves the overall sensitivity of the NV center (Eq. (C5)). Figure 3c shows the photoluminescence behavior of one of the NV centers involved in the experiment (table I, NV3). The collected

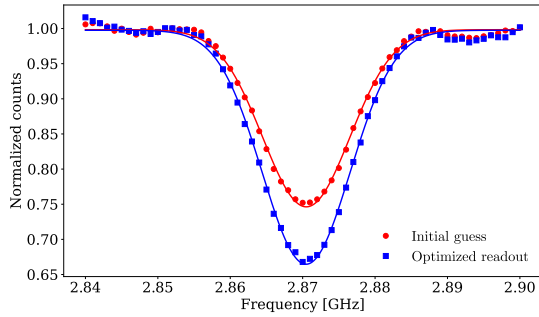


Figure 6. (color online) Pulsed ODMR at ZFS with optimized parameters using a rectangular MW π -pulse of the duration of 57 ns. The experiment with optimized laser parameters exhibits an improved contrast of ca. 0.33 (red) in comparison to the initial guess with a contrast of ca. 0.25 (blue).

Table I. Optimized parameters for spin state readout contrast with single NV centers. ZFS denotes the optimization performed in the absence of an external bias magnetic field. NV2 and NV3 related experiments are performed with a bias field of 12 mT.

Identifier	\mathcal{L}_p^{opt} [mW]	\mathcal{L}_d^{opt} [ns]	W_{ro}^{opt} [ns]	t_w^{opt} [ns]	Reference
NV1 (ZFS)	21	585	260	470	Fig. 6
NV2	17	488	250	270	Fig. 7
NV3	16	552	385	260	Fig. 1d, 8, 9, 10, 11

signal reflects the improvement in the average readout contrast after the optimization.

The optimized laser parameters are tested by combining them with a standard pulsed ODMR sequence with rectangular spin inversion pulses (pulse duration of 57 ns). Figure 6 shows a comparison between the measurement with and without optimized parameters (zero bias field, table I, NV2). The optimized parameters account for a 33% improvement in peak contrast. This result can be improved even further by also optimizing the spin inversion pulses.

B. Pulsed ODMR measurements with optimized MW pulse

Just as the laser pulse, the spin inversion pulse that is part of the pulsed ODMR protocol provides a target for further optimization. In this regard, we investigate the additional improvement by optimizing the pulses under a bias field B_{NV} to emulate a spin resonance sensing scenario. The FoM is calculated by averaging the contrast over a set of $N_p = 5$ measurements (see Eq. (10)) leading to control pulses in the range of 4% - 100% of the maximum control power (or equivalently, 20% - 100% of

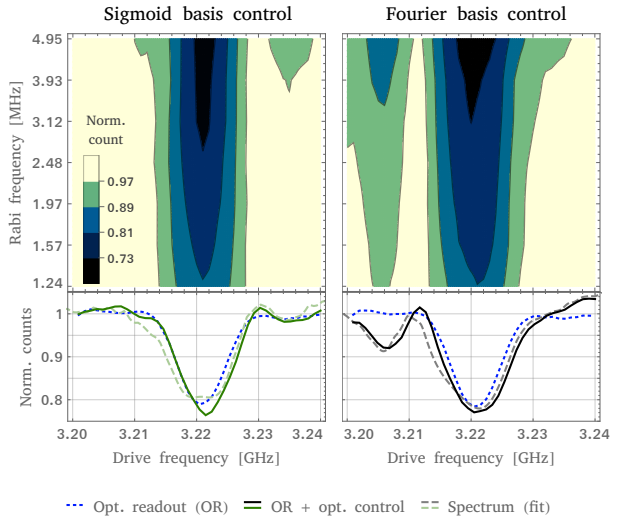


Figure 7. (color online) Comparison between two optimized spin inversion pulses in presence of a bias field $B_{NV} = 12$ mT (table I, NV2). The contrast is previously optimized according to Eq. (10) at the center frequency of 3.22 MHz. The left (right) side shows the results from a pulse optimized with the Sigmoid (Fourier) basis. The photon count is normalized with respect to the baseline. The top row shows the normalized count over a range of drive amplitudes (Rabi frequencies) and drive frequencies. The average over all Rabi frequencies is shown together with the equivalent values of the initial guess at the bottom. Both pulses exhibit robustness with respect to the amplitude variations, improving the contrast compared to the initial guess. However, the Sigmoid basis pulse is spectrally narrow, while the Fourier pulse has a distinct sideband. These features can be explained by the spectral shape of the pulses. The Fourier basis contains high-frequency elements caused by the cut-off limitation (see Fig. 5), which the Sigmoid basis avoided. The pulse spectra are convoluted with the NV's natural emission line and fitted to the normalized count to obtain the plots shown in the bottom panels.

the maximum control amplitude, i.e. Rabi frequency).

Figure 7 shows two maps representing the normalized count obtained with two optimized MW pulses. In this example, the laser pulses were pre-optimized according to the method described above, and the $m_s = 0 \leftrightarrow +1$ transition is used for the optimization as well as the assessment via pulsed ODMR. The pulse used to obtain the data on the left is optimized with the Fourier basis (pulse duration of 200 ns), while the data on the right follows an optimization with the Sigmoid basis (pulse duration of 200 ns). The Fourier pulse leads to a resonance profile with a side-band. Still, the Sigmoid pulse is approximately bandwidth-limited with only a single resonance peak as it mostly keeps its smooth form while providing a sufficient pulse area. Robustness against amplitude variations is relevant for applications that involve control power variation. The NV center experiences the variations according to its relative distance from the MW antenna, e.g. due to the movement of the cantilever in

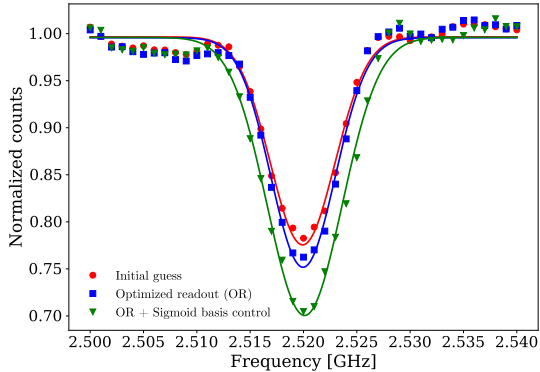


Figure 8. (color online) Pulsed ODMR in presence of a bias magnetic field ($B_{\text{NV}} \approx 12$ mT, NV3 from table I) with optimized laser parameters and MW pulses. Following the results from Fig. 7 the optimization was done with the Sigmoid basis, using the bandwidth-limited restriction approach. The data shows the improvement in contrast with each step of the optimization. The initial contrast for the resonance peaks is ca. 0.22 (initial guess, red), which is further improved to ca. 0.24 with optimized laser parameters (blue). The MW pulse optimized in the Sigmoid basis on top improves the contrast to ca. 0.30 (green). The solid lines show the Gaussian fits for the respective data (see appendix C).

diamond-based scanning probe applications [63].

To test the general applicability of this method for generating bandwidth-limited control pulses, similar optimization and pulsed ODMR experiments are performed with a different NV center (table I, NV3), this time using the $m_s = 0 \leftrightarrow -1$ transition, and the bandwidth-limited approach (Fig. 5). The results are shown in Fig. 8. Here, a readout contrast of ca. 0.24 is obtained with optimized laser parameters (pulse duration of 130 ns). The Sigmoid pulse (pulse duration of 200 ns) enhances the readout contrast further to ca. 0.30. Pulsed ODMR experiments with different peak control power are performed to test the robustness of the control pulse. The readout contrast and FWHM are obtained by fitting the data with a Gaussian profile.

Figure 9 shows the achievable average sensitivity of the pulsed ODMR method. It depends on the resonance profile, its FWHM, contrast, and the measurement time involved in the experiment (see Eq. (C5)). In addition, the spin projection noise sets a lower limit to the sensitivity. The full optimization, including the laser parameters and the robust Sigmoid pulse, leads to a sub- $\mu\text{T Hz}^{-\frac{1}{2}}$ average sensitivity considering up to almost 83% variation in the control power (see appendix C for details on the sensitivity calculation). Such robustness enables the sensing of larger micro-structures increasing the explorable sample dimension by few hundreds of μm , in addition to advantages offered by optimized MW antenna designs [57, 64]. Similar enhancements apply to wire or loop-antenna-based applications [65, 66], where QOC-based methods have been previously explored [36, 67]. This is also directly applicable to NV-based wide-field

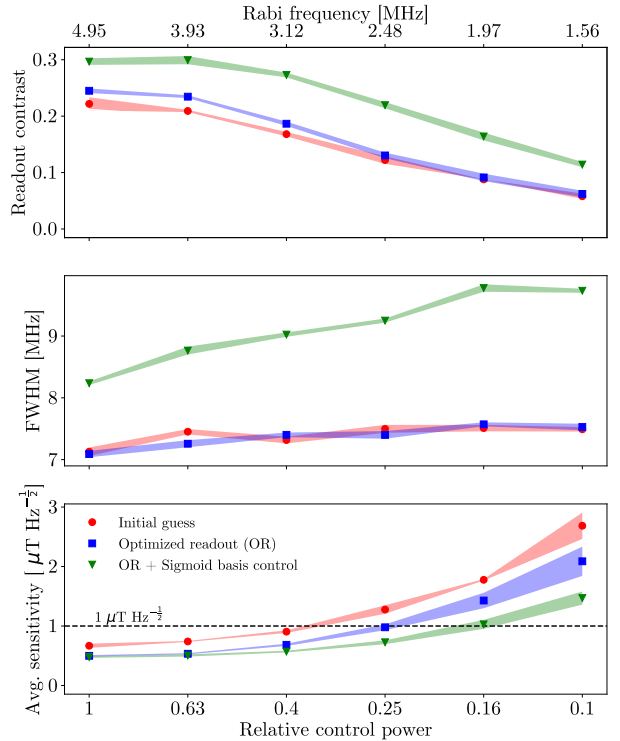


Figure 9. (color online) Comparison of pulsed ODMR measurements with optimized and standard spin state inversion pulses (NV3 from table I). Specifically, the robustness against amplitude variation is shown for pulses optimized in the Sigmoid basis. From top to bottom, the contrast, and FWHM of the resonance peaks as well as the corresponding average sensitivity are shown. All results are obtained with different amplitude variations. The red curves indicate the initial guess. Blue curves correspond to the experiments performed with optimized spin readout parameters. The green curves show the results for the experiments using optimized MW pulses. The dashed line in the bottom plot shows the ceiling for the sensitivity of $\mu\text{T Hz}^{-\frac{1}{2}}$.

imaging methods with ensembles of NV centers [68, 69]. Here, a robust excitation pulse over a large interrogation volume has the advantage of improved readout counts, and in turn, enhanced sensitivity [5].

Off-axial magnetic field components lead to spin-mixing, reducing the readout contrast [62]. This effect becomes apparent when comparing the contrast at ZFS (Fig. 6) and in presence of an external magnetic field (Fig. 8). The degree of spin-mixing, and hence its effects on the transition rates cannot be straightforwardly simulated for the presented experiments. Using closed-loop optimization of the laser pulse parameters allows to nevertheless incorporate such effects into the FoM.

Up to this point, all three NV centers from table I were investigated. As the improvements are of the same order of magnitude, only NV3 is considered in the following without loss of generality. The Ramsey sequence, which is addressed next, fulfills a similar role to the pulsed ODMR sequence, and additionally offers better sensitivities to-

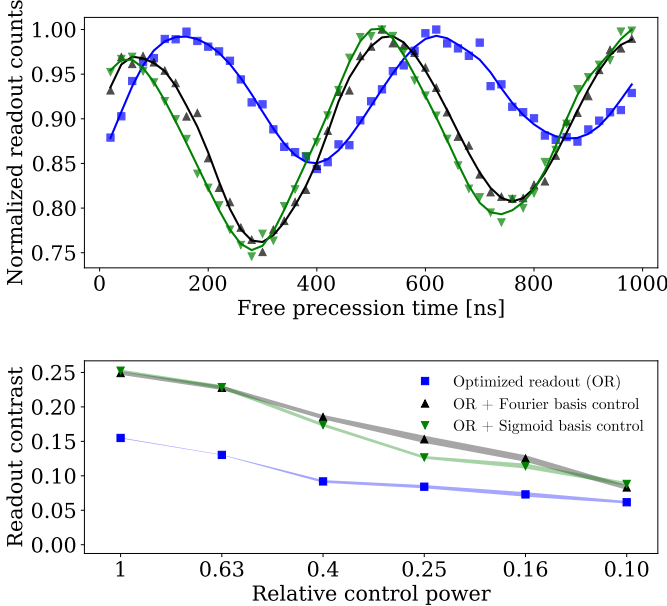


Figure 10. (Color online) Optimized Ramsey measurements. The top plot shows the measurements performed at peak drive power with rectangular control pulses (blue) as well as optimized pulses in the Fourier basis (black) and Sigmoid basis (green). The optimized pulses exhibit almost double the contrast in comparison to the rectangular control pulse. The length of the rectangular $\frac{\pi}{2}$ -pulse is determined by performing Rabi measurements, and in this case is 67 ns. The bottom plot shows the variation in readout contrast with respect to the change in relative control power of the control pulse. The performance of the robust optimized pulses surpasses the rectangular control pulse over the entire range of tested control power (90% variation).

wards external DC magnetic fields.

C. Ramsey Measurement

The Ramsey method is a type of interference measurement for DC magnetic fields. As discussed in section II it consists of two $\frac{\pi}{2}$ -pulses and offers a higher sensitivity in comparison to the ODMR methods. The $\frac{\pi}{2}$ -pulses are optimized via assessment of the contrast for a range of drive amplitudes (see Eq. (11)) via the bandwidth-limited approach discussed in section III B (see Fig. 5). The resulting interference fringes are shown in Fig. 10. This optimization is carried out in presence of a bias external magnetic field ($B_{NV} = 12$ mT) and on-resonance with the $m_s = 0 \leftrightarrow -1$ transition. The fringe visibility is enhanced from 0.15 to ca. 0.24 with the Fourier basis pulse (pulse duration of 100 ns), and to ca. 0.25 with the Sigmoid basis pulse (pulse duration of 100 ns) using the maximum control amplitude. The fringe visibility is directly related to the readout contrast. An improvement in the readout contrast leads to a proportional improvement in the sensitivity of the sensor (see Eq. (C7)).

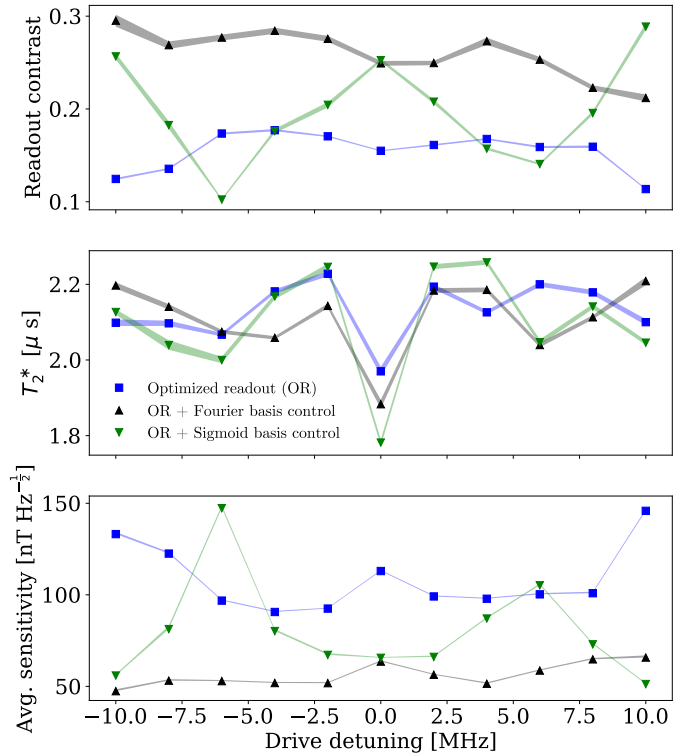


Figure 11. (color online) Comparison of Ramsey sequences with standard and optimized MW $\frac{\pi}{2}$ -pulses. All measurements are performed with optimized laser pulses for the readout and the optimizations were carried out with the amplitude-robust FoM from Eq. (11). The performance of the pulses optimized with the Fourier (black) and Sigmoid (green) basis is compared to the rectangular control pulse (blue) over a range of drive detunings. This range is equivalent to a variation of 0.35 mT in the external magnetic field. The upper panel shows the readout contrast \bar{C} . The respective T_2^* values are displayed in the middle panel. The bottom panel shows the resulting average sensitivity. The sensitivity calculation is discussed in appendix C.

The performance of the optimized pulses is further tested by performing Ramsey measurements with different drive frequencies in the vicinity of the spin transition frequency. These detunings correspond to a range of fields that could be measured in a sensing setup. The resulting readout signal summed over repeated iterations of the experiment is assessed for average sensitivity [10] of the NV center. The sensitivity of the Ramsey sequence depends on the readout contrast and the dephasing time during the measurements (see appendix C). Figure 11 shows the readout contrasts, the T_2^* -times, and the average sensitivities obtained by a series of Ramsey measurements. The Fourier pulse displays a constant readout contrast in the frequency range of ± 10 MHz. This range in the frequency corresponds to around ± 0.35 mT of variation in B_{NV} . In comparison, the Sigmoid pulse shows a marginally better \bar{C} around the resonance frequency but varies strongly for different detunings. The

frequency components of the pulse depend on the pulse shape (see appendix B). Here, the spectrum of the Sigmoid pulse contains minima at a detuning of approximately ± 5 MHz (Fig. 11). From a control perspective, such frequency selective applications are attractive for spectral hole burning [70] and quantum logic gates for superconducting qubits [71]. The T_2^* -time is comparatively lower on resonance than off resonance for all pulses. This is due to the destructive interference of the hyperfine transition associated with the spin resonance [72]. Readout contrast enhancement inherently involves strong contributions from all the hyperfine transitions, resulting in a trade-off between \bar{C} and T_2^* . The measurements with the Fourier pulse exhibit a robust average sensitivity of less than $65 \text{ nT Hz}^{-\frac{1}{2}}$. Such sensitivities are on par with single NV-based diamond scanning probes [63, 73]. In addition, such a robustness offers a range of working drive frequencies for operating the quantum sensor in slope detection mode [4] for DC field sensing.

The method from this section could be generalized to replace the spin-refocusing π -pulse in other sensing methods. This would require applying the optimized $\frac{\pi}{2}$ -pulses twice, using a strategy similar to the one discussed in section III B. Such refocusing pulses form the main building block for AC magnetic field sensing [6].

V. CONCLUSION

The optimizations in this work focused on three essential parts of quantum sensing with NV centers: optical spin state readout, population inversion, and $\frac{\pi}{2}$ -pulses. All three were improved for sensing methods with single NV centers considering control amplitude variations of up to 80%. The resulting protocols are realized by replacing the building blocks of common laser- and MW-based schemes with optimized equivalents. The optimizations are based on a set of figures of merit which are directly measurable via contrast using a varying MW power. The feedback-based approach inherently takes experimental imperfections and unknown system param-

eters into account. Initially, we optimized the optical readout/initialization process, improving the spin readout contrast by 32% in comparison to the standard protocol. Moreover, optimizing the spin inversion pulse in a pulsed ODMR protocol allowed for a further contrast improvement by 36% leading to sub $\mu\text{T Hz}^{-\frac{1}{2}}$ sensitivity that is maintained over a large range of MW amplitudes. To maintain frequency sensitivity, different optimization bases were explored. Additionally, we obtained an optimized $\frac{\pi}{2}$ -pulse for Ramsey measurements, enhancing the fringe contrast by 67% with respect to the square pulse with pre-optimized optical readout at maximum control power. Consequently, we obtained a consistent average sensitivity well below $100 \text{ nT Hz}^{-\frac{1}{2}}$ over a set of induced bias field strengths. While we applied the optimization to shallow NV centers, the approach is straightforwardly applicable to other NV-based systems like diamond scanning probes and NV ensembles used for wide-field imaging where similar control robustness features are required.

ACKNOWLEDGMENTS

We thank A. Marshall, F. Motzoi, R. Nelz, S. Z. Ahmed, T. Reisser and M. Rossignolo for their insights and suggestions. We furthermore thank T. Reisser for his assistance with the RedCRAB software suite. This work has received funding from the European Union's Horizon 2020 research and innovation programme under the Marie Skłodowska-Curie grant agreement N° 765267 (QuSCo) and under the grant agreement N° 820394 (ASTERIQS).

Authors' contributions: NO and EN planned the experiments. PR, NO, and MM planned the optimization strategies and worked to facilitate the remote optimization. NO designed and performed the experiments and analyzed the data. TC, SM, EN and MM supervised the project. All the authors discussed the results and contributed to the manuscript.

[1] In this manuscript the term NV center denotes the negatively charged state of the nitrogen-vacancy center in diamond.

[2] F. Jelezko and J. Wrachtrup, Single defect centres in diamond: A review, *physica status solidi (a)* **203**, 3207 (2006).

[3] M. W. Doherty, N. B. Manson, P. Delaney, F. Jelezko, J. Wrachtrup, and L. C. Hollenberg, The nitrogen-vacancy colour centre in diamond, *Physics Reports* **528**, 1 (2013).

[4] C. L. Degen, F. Reinhard, and P. Cappellaro, Quantum sensing, *Reviews of Modern Physics* **89**, 1 (2017).

[5] J. F. Barry, J. M. Schloss, E. Bauch, M. J. Turner, C. A. Hart, L. M. Pham, and R. L. Walsworth, Sensitivity optimization for nv-diamond magnetometry, *Reviews of Modern Physics* **92**, 015004 (2020).

[6] P. Rembold, N. Oshnik, M. M. Müller, S. Montangero, T. Calarco, and E. Neu, Introduction to quantum optimal control for quantum sensing with nitrogen-vacancy centers in diamond, *AVS Quantum Science* **2**, 024701 (2020).

[7] L. Childress, J. M. Taylor, A. S. Sørensen, and M. D. Lukin, Fault-tolerant quantum communication based on solid-state photon emitters, *Physical Review Letters* **96** (2006).

[8] G. Balasubramanian, I. Y. Chan, R. Kolesov, M. Al-Hmoud, J. Tisler, C. Shin, C. Kim, A. Wojcik, P. R. Hemmer, A. Krueger, T. Hanke, A. Leitenstorfer, R. Bratschitsch, F. Jelezko, and J. Wrachtrup, Nanoscale imaging

magnetometry with diamond spins under ambient conditions, *Nature* **455**, 648 (2008).

[9] J. R. Maze, P. L. Stanwick, J. S. Hodges, S. Hong, J. M. Taylor, P. Cappellaro, L. Jiang, M. V. G. Dutt, E. Togan, A. S. Zibrov, A. Yacoby, R. L. Walsworth, and M. D. Lukin, Nanoscale magnetic sensing with an individual electronic spin in diamond, *Nature* **455**, 644 (2008).

[10] J. M. Taylor, P. Cappellaro, L. Childress, L. Jiang, D. Budker, P. R. Hemmer, A. Yacoby, R. Walsworth, and M. D. Lukin, High-sensitivity diamond magnetometer with nanoscale resolution, *Nature Physics* **4**, 810 (2008).

[11] F. Dolde, H. Fedder, M. W. Doherty, T. Nöbauer, F. Rempp, G. Balasubramanian, T. Wolf, F. Reinhard, L. C. L. Hollenberg, F. Jelezko, and J. Wrachtrup, Electric-field sensing using single diamond spins, *Nature Physics* **7**, 459 (2011).

[12] V. M. Acosta, E. Bauch, M. P. Ledbetter, A. Waxman, L.-S. Bouchard, and D. Budker, Temperature dependence of the nitrogen-vacancy magnetic resonance in diamond, *Physical Review Letters* **104**, 070801 (2010).

[13] P. Konzelmann, T. Rendler, V. Bergholm, A. Zappe, V. Pfannenstill, M. Garsi, F. Ziem, M. Niethammer, M. Widmann, S. Y. Lee, P. Neumann, and J. Wrachtrup, Robust and efficient quantum optimal control of spin probes in a complex (biological) environment. Towards sensing of fast temperature fluctuations, *New Journal of Physics* **20** (2018).

[14] M. W. Doherty, V. V. Struzhkin, D. A. Simpson, L. P. McGuinness, Y. Meng, A. Stacey, T. J. Karle, R. J. Hemley, N. B. Manson, L. C. Hollenberg, and S. Prawer, Electronic properties and metrology applications of the diamond nv center under pressure, *Physical Review Letters* **112**, 047601 (2014).

[15] M. Lesik, T. Plisson, L. Toraille, J. Renaud, F. Occelli, M. Schmidt, O. Salord, A. Delobbe, T. Debuisschert, L. Rondin, P. Loubeyre, and J.-F. Roch, Magnetic measurements on micrometer-sized samples under high pressure using designed NV centers, *Science* **366**, 1359 (2019).

[16] G. D. Fuchs, G. Burkard, P. V. Klimov, and D. D. Awschalom, A quantum memory intrinsic to single nitrogen-vacancy centres in diamond, *Nature Physics* **7**, 789 (2011).

[17] C. E. Bradley, J. Randall, M. H. Abobeih, R. C. Berrevoets, M. J. Degen, M. A. Bakker, M. Markham, D. J. Twitchen, and T. H. Taminiau, A Ten-Qubit Solid-State Spin Register with Quantum Memory up to One Minute, *Physical Review X* **9**, 031045 (2019).

[18] G. Balasubramanian, P. Neumann, D. Twitchen, M. Markham, R. Kolesov, N. Mizuochi, J. Isoya, J. Achard, J. Beck, J. Tissler, V. Jacques, P. R. Hemmer, F. Jelezko, and J. Wrachtrup, Ultralong spin coherence time in isotopically engineered diamond, *Nature Materials* **8**, 383 (2009).

[19] C. L. Degen, Scanning magnetic field microscope with a diamond single-spin sensor, *Applied Physics Letters* **92**, 243111 (2008).

[20] D. Bluvstein, Z. Zhang, and A. C. B. Jayich, Identifying and mitigating charge instabilities in shallow diamond nitrogen-vacancy centers, *Physical Review Letters* **122**, 076101 (2019).

[21] C. Osterkamp, M. Mangold, J. Lang, P. Balasubramanian, T. Teraji, B. Naydenov, and F. Jelezko, Engineering preferentially-aligned nitrogen-vacancy centre ensembles in CVD grown diamond, *Scientific Reports* **9**, 1 (2019).

[22] M. Schreck, S. Gsell, R. Brescia, and M. Fischer, Ion bombardment induced buried lateral growth: The key mechanism for the synthesis of single crystal diamond wafers, *Scientific Reports* **7**, 1 (2017).

[23] L. M. K. Vandersypen and I. L. Chuang, NMR techniques for quantum control and computation, *Reviews of Modern Physics* **76**, 1037 (2005).

[24] S. J. Glaser, U. Boscain, T. Calarco, C. P. Koch, W. Köckenberger, R. Kosloff, I. Kuprov, B. Luy, S. Schirmer, T. Schulte-Herbrüggen, D. Sugny, and F. K. Wilhelm, Training Schrödinger's cat: Quantum optimal control: Strategic report on current status, visions and goals for research in Europe, *European Physical Journal D* **69** (2015).

[25] M. M. Müller, R. S. Said, F. Jelezko, T. Calarco, and S. Montangero, One decade of quantum optimal control in the chopped random basis, *arXiv:2104.07687 [quant-ph]* (2021).

[26] R. Schirhagl, K. Chang, M. Loretz, and C. L. Degen, Nitrogen-vacancy centers in diamond: Nanoscale sensors for physics and biology, *Annual Review of Physical Chemistry* **65**, 83 (2014).

[27] N. Mohan, C.-S. Chen, H.-H. Hsieh, Y.-C. Wu, and H.-C. Chang, In vivo imaging and toxicity assessments of fluorescent nanodiamonds in *caenorhabditis elegans*, *Nano Letters* **10**, 3692 (2010).

[28] R. Nelz, M. Radtke, A. Slablab, Z.-Q. Xu, M. Kianinia, C. Li, C. Bradac, I. Aharonovich, and E. Neu, Near-field energy transfer between a luminescent 2d material and color centers in diamond, *Advanced Quantum Technologies* **3**, 1900088 (2020).

[29] Thorlabs, Parts: C6w, cp08/m, cp02t/m, ersca, er1, cp90f (2021), accessed on: 30.11.2020.

[30] GrabCAD, *Coaxial connector design by avitek, coaxial cable design by steven minichiello, and objective design by thorfynn.* (2021), accessed on: 07.06.2021.

[31] B. K. Ofori-Okai, S. Pezzagna, K. Chang, M. Loretz, R. Schirhagl, Y. Tao, B. A. Moores, K. Groot-Berning, J. Meijer, and C. L. Degen, Spin properties of very shallow nitrogen vacancy defects in diamond, *Physical Review B* **86**, 081406 (2012).

[32] Y. Romach, C. Müller, T. Unden, L. J. Rogers, T. Isoda, K. M. Itoh, M. Markham, A. Stacey, J. Meijer, S. Pezzagna, B. Naydenov, L. P. McGuinness, N. Bar-Gill, and F. Jelezko, Spectroscopy of surface-induced noise using shallow spins in diamond, *Physical Review Letters* **114**, 017601 (2015).

[33] S. Hernández-Gómez and N. Fabbri, Quantum control for nanoscale spectroscopy with diamond nitrogen-vacancy centers: A short review, *Frontiers in Physics* **8**, 652 (2021).

[34] F. Poggiali, P. Cappellaro, and N. Fabbri, Optimal Control for One-Qubit Quantum Sensing, *Physical Review X* **8** (2018).

[35] A. F. L. Poulsen, J. D. Clement, J. L. Webb, R. H. Jensen, K. Berg-Sørensen, A. Huck, and U. L. Andersen, Optimal control of a nitrogen-vacancy spin ensemble in diamond for sensing in the pulsed domain, *arXiv:2101.10049 [quant-ph]* (2021).

[36] T. Nöbauer, A. Angerer, B. Bartels, M. Trupke, S. Rotter, J. Schmiedmayer, F. Mintert, and J. Majer, Smooth Optimal Quantum Control for Robust Solid-State Spin Magnetometry, *Physical Review Letters* **115**, 190801

(2015).

[37] F. Ziem, M. Garsi, H. Fedder, and J. Wrachtrup, Quantitative nanoscale mri with a wide field of view, *Scientific Reports* **9**, 12166 (2019).

[38] T. Häberle, D. Schmid-Lorch, K. Karrai, F. Reinhard, and J. Wrachtrup, High-dynamic-range imaging of nanoscale magnetic fields using optimal control of a single qubit, *Physical Review Letters* **111**, 170801 (2013).

[39] N. Khaneja, T. Reiss, C. Kehlet, T. Schulte-Herbrüggen, and S. J. Glaser, Optimal control of coupled spin dynamics: Design of NMR pulse sequences by gradient ascent algorithms, *Journal of Magnetic Resonance* **172**, 296 (2005).

[40] S. Machnes, U. Sander, S. J. Glaser, P. Defouquié, A. Gruslys, S. Schirmer, T. Schulte-Herbrüggen, P. de Fouquières, A. Gruslys, S. Schirmer, and T. Schulte-Herbrüggen, Comparing, optimizing, and benchmarking quantum-control algorithms in a unifying programming framework, *Physical Review A* **84**, 22305 (2011).

[41] A. I. Konnov and V. F. Krotov, On global methods for the successive improvement of control processes, *Avtomatika i Telemekhanika* **60**, 77 (1999).

[42] M. H. Goerz, D. Basilewitsch, F. Gago-Encinas, M. G. Krauss, K. P. Horn, D. M. Reich, and C. P. Koch, Krotov: A Python implementation of Krotov's method for quantum optimal control, *SciPost Physics* **7**, 80 (2019).

[43] P. Doria, T. Calarco, and S. Montangero, Optimal Control Technique for Many-Body Quantum Dynamics, *Physical Review Letters* **106**, 190501 (2011).

[44] N. Rach, M. M. Müller, T. Calarco, and S. Montangero, Dressing the chopped-random-basis optimization: A bandwidth-limited access to the trap-free landscape, *Physical Review A* **92**, 62343 (2015).

[45] J. J. Sørensen, J. H. M. Jensen, T. Heinzel, and J. F. Sherson, QEngine: A C++ library for quantum optimal control of ultracold atoms, *Computer Physics Communications* **243**, 135 (2019).

[46] S. Machnes, E. Assémat, D. Tannor, and F. K. Wilhelm, Tunable, Flexible, and Efficient Optimization of Control Pulses for Practical Qubits, *Physical Review Letters* **120**, 150401 (2018).

[47] S. Lloyd and S. Montangero, Information theoretical analysis of quantum optimal control, *Physical Review Letters* **113**, 1 (2014).

[48] M. M. Müller, S. Gherardini, T. Calarco, S. Montangero, and F. Caruso, Information theoretical limits for quantum optimal control solutions: Error scaling of noisy channels (2020), [arXiv:2006.16113 \[quant-ph\]](https://arxiv.org/abs/2006.16113).

[49] L. M. Rios and N. V. Sahinidis, Derivative-free optimization: a review of algorithms and comparison of software implementations, *Journal of Global Optimization* **56**, 1247 (2013).

[50] R. Heck, O. Vuculescu, J. J. Sørensen, J. Zoller, M. G. Andreassen, M. G. Bason, P. Ejlertsen, O. Elfasson, P. Haikka, J. S. Laustsen, L. L. Nielsen, A. Mao, R. Müller, M. Napolitano, M. K. Pedersen, A. R. Thorsen, C. Bergenholtz, T. Calarco, S. Montangero, and J. F. Sherson, Remote optimization of an ultracold atoms experiment by experts and citizen scientists, *Proceedings of the National Academy of Sciences of the United States of America* **115**, E11231 (2018).

[51] J. A. Nelder and R. Mead, A Simplex Method for Function Minimization, *The Computer Journal* **7**, 308 (1965).

[52] A. Dréau, M. Lesik, L. Rondin, P. Spinicelli, O. Arcizet, J.-F. Roch, and V. Jacques, Avoiding power broadening in optically detected magnetic resonance of single nv defects for enhanced dc magnetic field sensitivity, *Physical Review B* **84**, 195204 (2011).

[53] T. Caneva, T. Calarco, and S. Montangero, Chopped random-basis quantum optimization, *Physical Review A* **84**, 22326 (2011).

[54] P. Rembold, M. Müller, T. Calarco, and S. Montangero, Manuscript in preparation (2021).

[55] V. M. Acosta, E. Bauch, M. P. Ledbetter, C. Santori, K.-M. C. Fu, P. E. Barclay, R. G. Beausoleil, H. Linget, J. F. Roch, F. Treussart, S. Chemerisov, W. Gawlik, and D. Budker, Diamonds with a high density of nitrogen-vacancy centers for magnetometry applications, *Physical Review B* **80**, 115202 (2009).

[56] D. Budker, D. Kimball, and D. DeMille, *Atomic physics: An exploration through problems and solutions*, second edition ed. (Oxford University Press, Oxford, New York, 2008).

[57] O. R. Opaluch, N. Oshnik, R. Nelz, and E. Neu, Optimized planar microwave antenna for nitrogen vacancy center based sensing applications, *Nanomaterials* **11** (2021).

[58] B. J. Shields, Q. P. Unterreithmeier, N. P. de Leon, H. Park, and M. D. Lukin, Efficient readout of a single spin state in diamond via spin-to-charge conversion, *Physical Review Letters* **114**, 136402 (2015).

[59] N. Aslam, G. Waldherr, P. Neumann, F. Jelezko, and J. Wrachtrup, Photo-induced ionization dynamics of the nitrogen vacancy defect in diamond investigated by single-shot charge state detection, *New Journal of Physics* **15**, 013064 (2013).

[60] T. Rendler, *Fluorescent nanodiamonds as a sensor and life science probe*, Ph.D. thesis, Faculty of Mathematics and Physics, University of Stuttgart, The address of the publisher (2018), accepted: 2018-04-10T13:41:13Z.

[61] E. Bourgeois, A. Jarmola, P. Siyushev, M. Gulk, J. Hruba, F. Jelezko, D. Budker, and M. Nesladek, Photoelectric detection of electron spin resonance of nitrogen-vacancy centres in diamond, *Nature Communications* **6**, 8577 (2015).

[62] J.-P. Tetienne, L. Rondin, P. Spinicelli, M. Chipaux, T. Debuisschert, J.-F. Roch, and V. Jacques, Magnetic-field-dependent photodynamics of single NV defects in diamond: an application to qualitative all-optical magnetic imaging, *New Journal of Physics* **14**, 103033 (2012).

[63] M. Radtke, E. Bernardi, A. Slablab, R. Nelz, and E. Neu, Nanoscale sensing based on nitrogen vacancy centers in single crystal diamond and nanodiamonds: achievements and challenges, *Nano Futures* **3**, 042004 (2019).

[64] K. Sasaki, Y. Monnai, S. Saijo, R. Fujita, H. Watanabe, J. Ishi-Hayase, K. M. Itoh, and E. Abe, Broadband, large-area microwave antenna for optically detected magnetic resonance of nitrogen-vacancy centers in diamond, *Review of Scientific Instruments* **87**, 053904 (2016).

[65] M. E. Trusheim and D. Englund, Wide-field strain imaging with preferentially aligned nitrogen-vacancy centers in polycrystalline diamond, *New Journal of Physics* **18**, 123023 (2016).

[66] J. M. Schloss, J. F. Barry, M. J. Turner, and R. L. Walsworth, Simultaneous broadband vector magnetometry using solid-state spins, *Physical Review Applied* **10**, 034044 (2018).

- [67] F. Ziem, M. Garsi, H. Fedder, and J. Wrachtrup, Quantitative nanoscale MRI with a wide field of view, *Scientific Reports* **9**, 12166 (2019).
- [68] Y. Schlussel, T. Lenz, D. Rohner, Y. Bar-Haim, L. Bougas, D. Groswasser, M. Kieschnick, E. Rozenberg, L. Thiel, A. Waxman, J. Meijer, P. Maletinsky, D. Budker, and R. Folman, Wide-field imaging of superconductor vortices with electron spins in diamond, *Physical Review Applied* **10**, 034032 (2018).
- [69] M. Chipaux, A. Tallaire, J. Achard, S. Pezzagna, J. Meijer, V. Jacques, J.-F. Roch, and T. Debuisschert, Magnetic imaging with an ensemble of nitrogen-vacancy centers in diamond, *The European Physical Journal D* **69**, 166 (2015).
- [70] C. J. Foot, *Atomic Physics*, Oxford Master Series in Physics (Oxford University Press, Oxford, New York, 2005).
- [71] L. S. Theis, F. Motzoi, S. Machnes, and F. K. Wilhelm, Counteracting systems of diabaticities using DRAG controls: The status after 10 years, *Europhysics Letters* **123**, 60001 (2018).
- [72] T. D. Ladd, F. Jelezko, R. Laflamme, Y. Nakamura, C. Monroe, and J. L. O'Brien, Quantum computers, *Nature* **464**, 45 (2010).
- [73] Q.-C. Sun, T. Song, E. Anderson, A. Brunner, J. Förster, T. Shalomayeva, T. Taniguchi, K. Watanabe, J. Gräfe, R. Stöhr, X. Xu, and J. Wrachtrup, Magnetic domains and domain wall pinning in atomically thin crbr3 revealed by nanoscale imaging, *Nature Communications* **12**, 1989 (2021).
- [74] D. Budker and M. G. Kozlov, Sensing: Equation one, [arXiv:2011.11043 \[quant-ph\]](https://arxiv.org/abs/2011.11043) (2020).

Appendix A: Experimental setup

All the measurements were carried out on a custom built confocal setup, with excitation wavelength of 520 nm (Swabian instruments, DL nSec, PE 520) and objective numerical aperture of 0.8 (Olympus, LM-PLFLN100X). Rejection of the out-of-focus fluorescence signal was achieved by using single mode optical fibers (Thorlabs, SM450 and SM600) at the excitation and detection arm of the confocal microscope. Futher, contributions from the NV^0 charge state was blocked with a spectral filter (Thorlabs, FEL0600, Longpass 600 nm) in the detection arm. Fluorescence signal from the single NVs was detected with a single photon counting module (APD, Excelitas, SPCM-AQRH-14, quantum efficiency $\approx 68\%$) and the acquired data was logged with a data acquisition card (National Instruments, PCIe-6323). Second order intensity correlation measurements were performed with a Hanbury-Brown Twiss setup attached to a time resolved counting device (PicoQuant, PicoHarp 300). The fluorescence signal was filtered and analyzed with a spectrometer (Princeton Instruments) to ensure the charge state stability in the diamond sample. The MW control pulses were generated with IQ mixing with the MW signal generator source (Tektronix 4104A, IF bandwidth - 400 MHz). The in-phase and quadrature components were obtained with an arbitrary waveform

generator (AWG, Tabor 1204 A, 2.3 GSa s $^{-1}$). Control pulses were delivered to the diamond sample with a custom built Ω -shaped antenna [57] after amplification (ZHL-16W-43-S+, Mini-Circuits, typ. +45 dB). Channel synchronization was ensured using a sync device (Swabian Instruments, Pulse Streamer 8/2) to trigger the diode laser, AWG, MW source, APD count window and the data acquisition device. The sample along with the MW-antenna was mounted onto a piezo-scanner (Physik Instrumente (PI), P-611.3O) to perform the confocal scans and address individual NV centers. The remote connection to the optimization server was obtained via combination of MATLAB (remote system) and Python (RedCRAB GUI) based control programs.

Appendix B: Random bases for dCRAB optimization

In the dCRAB algorithm, random bases are used whose elements can be defined through a superparameter ω which stays constant throughout the optimization. In this work, we have used two different bases, referred to as the Fourier and the Sigmoid basis. They differ in their shape and properties.

The Fourier basis is most commonly used with dCRAB. It consists of $M = 2$ out of phase trigonometric elements with frequency $0 \leq \omega \leq \omega_{\max}$:

$$\begin{aligned} f_{\text{Fourier}}^1(\omega; t) &= \sin(\omega t) \\ f_{\text{Fourier}}^2(\omega; t) &= \cos(\omega t). \end{aligned} \quad (\text{B1})$$

The Sigmoid basis [54] consists of sigmoid functions ($M = 1$) with an offset of $\epsilon\sigma \leq \omega \leq t_p - \epsilon\sigma$. ϵ represents an offset factor. The basis always includes one element at $\omega = \epsilon\sigma$ which is optimized in every superiteration to ensure the pulse length is constant (i.e. $u_i(t = 0) = u_i(t = t_p) = 0$). For the same reason, an element is added automatically with $\omega = t_p - \epsilon\sigma$ and amplitude $A = \sum_n^N A_n$.

$$f_{\text{Sigmoid}}(\omega; t) = \frac{1}{\sqrt{2\pi}\sigma} \int_0^t e^{-\frac{1}{2}(\frac{\tau-\omega}{\sigma})^2} d\tau. \quad (\text{B2})$$

They both have different properties. In general, the Fourier basis is bandwidth-limited through the upper limit for ω . The Sigmoid basis is bandwidth-limited due to the limited rise time defined by σ . However, in both cases higher frequency terms may be introduced through cut-offs (i.e. cut-offs in the time domain or amplitude domain).

It should also be noted that the basis choice determines which shapes are complex, and which are simple to produce. While the Fourier basis produces oscillations with few basis elements, the Sigmoid basis produces approximately square pulses, without cut-offs.

Appendix C: Sensitivity Calculation

NV center-based sensing is fundamentally limited by the spin projection limit [74]. This limit can be expressed as

$$\eta_{sp} = \frac{\hbar}{Sg_e\mu_B} \frac{1}{\sqrt{t_m}}, \quad (\text{C1})$$

where, \hbar is the reduced Plank's constant, g_e is the Landé factor, μ_B is the Bohr magneton, and t_m is the measurement time. In addition, optical readout processors are subjected to photon shot noise that further adheres the sensitivity. For the averaged readout process discussed in section I, Eq. (1), the readout fidelity can be equivalently written as

$$\mathcal{F} = \sqrt{1 + \frac{1}{\bar{C}^2 R_{avg}}}. \quad (\text{C2})$$

\bar{C} is the average readout contrast between the two spin states of the system and R_{avg} is the average count rate. Further, an overhead cost is always involved in an experimental scenario. Really long spin initialization and readout duration deteriorates the overall sensitivity of the sensor, this can be expressed as a scaling factor for the sensitivity

$$\kappa_{exp} = \sqrt{\frac{t_m + 2 \times t_i}{t_m}}, \quad (\text{C3})$$

under the assumption that the initialization and readout duration are equal (t_i). Finally, for DC magnetometry methods, the dephasing time T_2^* further limits the sensitivity, this can be expressed the decoherence function of the T_2^* -limited processes,

$$f_d = e^{\left(\frac{t_m}{T_2^*}\right)^m}, \quad (\text{C4})$$

where, m is the order of decoherence. For spectroscopic measurement around the NV resonance peaks, the sensitivity depends on the resonance profile itself [5]. In case

of Gaussian resonance profiles for the pulsed ODMR measurements, the overall sensitivity can be computed as

$$\eta^{po} = \frac{8}{3\sqrt{3}} \frac{1}{\gamma_{NV}} \frac{\sigma_f}{\bar{C}\sqrt{R_{avg}}} \sqrt{T_\pi + t_m}. \quad (\text{C5})$$

Here, f_0 is the resonance peak, σ_f is the resonance peak FWHM, $\gamma_{NV} = \frac{g_e\mu_B}{\hbar}$, is the gyromagnetic ratio of the NV spin, and T_π is the pulse duration. For shorthand notation, the measurement time is assumed to involve the overhead experimental time $t_m = t_w + 2 \times t_i$. The relevant parameters for the sensitivity calculation in section IV were obtained by fitting the data with the following function:

$$I^{po}(f) = R_{avg} \times \left[1 - \bar{C} \times e^{-\frac{1}{2} \left(\frac{f-f_0}{\Delta f} \right)^2} \right]. \quad (\text{C6})$$

For a Gaussian profile, $\sigma_f = 2\sqrt{2\ln 2} \times \Delta f$. It is noteworthy that for pulsed ODMR measurements at low MW power, T_2^* -limit becomes relevant and has to be considered for sensitivity calculations, the reader is advised to refer to Ref. [52] for more details.

The average sensitivity for the Ramsey sequence-based methods can be expressed under the T_2^* -limit as,

$$\eta^{Ra} = \frac{1}{\bar{C}\gamma_{nv}\tau} \exp \left[\left(\frac{\tau}{T_2^*} \right)^m \right] \sqrt{\tau + t_m}. \quad (\text{C7})$$

The free induction decay of the Ramsey fringes for single NV centers highlight the hyperfine structure originating from the electron-nuclear spin coupling. Likewise, the related data can be fit with a sum of the three precessing hyperfine transitions,

$$I^{Ra}(t) = R_{avg} \left[1 + \left(\bar{C} \times e^{-\left(\frac{\tau}{T_2^*}\right)^m} \sum_i^3 A_i \cos(2\pi\nu_i t + \phi_i) \right) \right], \quad (\text{C8})$$

where, ν_i and ϕ_i are the precession frequency and phase corresponding to the hyperfine transitions. The sensitivities in Fig. 11 are obtained at $\tau = 0.5 \times T_2^*$.